



# In-situ constructing oxide-anion dual-layer on Ce-B-containing electrode electrolyte interface towards highly corrosive seawater splitting

Huixiang Liu<sup>a,b</sup>, Xian Zhou<sup>b</sup>, Chuming Ye<sup>a,b</sup>, Mingxin Ye<sup>a,\*</sup>, Jianfeng Shen<sup>a,\*</sup>

<sup>a</sup> Institute of Special Materials and Technology, Fudan University, Shanghai 200433, PR China

<sup>b</sup> Department of Materials Science, Fudan University, Shanghai 200433, PR China

## ARTICLE INFO

### Keywords:

Seawater electrocatalysis  
Boride  
Dual-layer protection  
Anti-corrosion  
Chloride ion

## ABSTRACT

Seawater electrocatalysis holds significant promise as a technology for sustainable energy production, but the challenge of electrode corrosion by chloride ions is urgently needed to be addressed. Herein, a Ce-B-containing electrode was found to activate an in-situ evolutionary oxide (CeO<sub>2</sub>)-anion (B(OH)<sub>4</sub><sup>-</sup>) dual-layer during the electrocatalytic reconstruction process, effectively resisting the invasion of chloride ions. In detail, a Ni-Fe-Ce-B electrode exhibits high hydrogen and oxygen evolution activity with only 160 and 271 mV overpotentials at 100 mA cm<sup>-2</sup> in 1 M KOH + 0.5 M NaCl, and superior stability with slight overpotential loss after over 100 h at industrial current density ~ 0.5 A cm<sup>-2</sup> at 1.817 V for alkaline natural seawater splitting. Comparative experiments indicating that existing alkaline electrocatalysts can be adjusted to withstand rigorous seawater conditions through straightforward modifications. This work reveals a novel evolutionary oxide-anion dual-layer protection mechanism to effectively prevent chloride ion corrosion in highly corrosive seawater splitting.

## 1. Introduction

Water electrolysis is an efficient technique for achieving high-purity hydrogen production without carbon emissions, thereby facilitating the achievement of targets such as “carbon peaking” and “carbon neutrality” [1]. However, excessive usage of scarce freshwater for industrial processes constraints sustainable water management and sustainability efforts. Seawater stands as one of most abundant natural resources, constituting a staggering 96.5 % of total water reserves [2,3]. Seawater electrocatalysis, which involves the electrochemical conversion of seawater into hydrogen and other valuable chemicals, has been gaining increasing attention as a promising technology for renewable energy production. During the process of seawater electrocatalysis at the anode, two competitive reactions transpire: the oxygen evolution reaction (OER) and the chlorine evolution reaction (ClER) [4]. Preventing the occurrence of ClER is crucial for achieving efficient seawater electrolysis. Fortunately, there exists a beneficial “alkaline design criterion” in seawater electrolysis. This criterion allows a water oxidation catalyst to operate with a kinetic overpotential of up to approximately 480 mV, all while avoiding any detrimental interference from chlorine chemistry [5]. Besides, the other severe challenge in this field is the collapse and corrosion of electrodes by the aggressive chloride ions, which can

significantly reduce the durability and efficiency of the system. They tend to corrode various catalytic electrodes through the following formation mechanisms of metal chloride-hydroxides [6].

Cl<sup>-</sup> adsorption facilitated through surface polarization:



Dissolution through additional coordination:



Transformation from chloride to hydroxide:



Till now, researchers have employed three primary strategies to develop anti-corrosion electrodes for seawater electrocatalysis (Fig. 1a). The first approach involves utilizing electrode materials that inherently possess anti-corrosion properties, such as RuO<sub>2</sub> and transition-metal (TM)-based catalysts [7]. However, the usage of these materials is limited due to their rarity and high cost, as well as their poor corrosion resistance and catalytic performance, making them unsuitable for large-scale applications. The second strategy entails the addition of buffer ions, such as PO<sub>4</sub><sup>3-</sup> [8] and SO<sub>4</sub><sup>2-</sup> [9], to the electrolyte. The buffer layer provides a barrier to chloride ions, albeit not entirely impervious,

\* Corresponding authors.

E-mail addresses: [mxye@fudan.edu.cn](mailto:mxye@fudan.edu.cn) (M. Ye), [jfshen@fudan.edu.cn](mailto:jfshen@fudan.edu.cn) (J. Shen).

<https://doi.org/10.1016/j.apcatb.2023.123560>

Received 21 September 2023; Received in revised form 10 November 2023; Accepted 23 November 2023

Available online 27 November 2023

0926-3373/© 2023 Elsevier B.V. All rights reserved.

which consequently puts a cap on the maximum achievable corrosion resistance. The third approach involves employing a physical layer on catalyst surface, such as a carbon layer or conductive polymer [10]. Regrettably, managing the additional coating thickness presents a significant challenge, which could potentially result in a compromise to the catalytic performance. In general, the constraints inherent in these strategies limit their aptness for practical utilization.

The current trend in laboratory research focuses on bestowing TM-based catalysts with chloride ion resistance through component manipulation and structural regulation [11–13]. As part of an emerging class, NiFe-based catalysts have displayed exceptional performance, especially its impressive OER ability [14]. Various composition optimization processes like sulfuration [6], nitridation [11], and phosphating [15] are utilized to tweak the crystal structure and facets, enhances the number of active sites or vacancies [16], leading to a significant reduction in the overpotential of OER. Furthermore, structural engineering approaches, such as multi-layers stacking [17] and creation of structural heterostructures [18], can modify or impede the path of chloride ion erosion. Urgently, fully exploring cheap and easily available NiFe-based catalysts can effectively balance the relationship between performance, economy, and sustainability [19].

Herein, we developed a novel evolutionary  $\text{CeO}_2\text{-B}(\text{OH})_4^-$  dual-layer strategy based on a Ni-Fe-Ce-B/MS electrode via a mild electroless plating for resisting chloride ion corrosion. In simulated alkaline seawater, Ni-Fe-Ce-B catalyst exhibits high hydrogen and oxygen evolution activity with only 160 and 271 mV at  $100 \text{ mA cm}^{-2}$ , even surpassing those of benchmark Pt/C and  $\text{IrO}_2$ , respectively. Impressively, it has been applied into the industrial alkaline natural seawater electrolysis in a two-electrode system, where an industrial current density of  $0.5 \text{ A cm}^{-2}$  can be realized at only 1.817 V with stability over 100 h for alkaline seawater splitting. During the electrocatalytic process, Ce is preferentially oxidized to form an oxide protective layer ( $\text{CeO}_2$ ) outside the catalyst, while B is dissolved and converted into borate buffer anions ( $\text{B}(\text{OH})_4^-$ ) (Fig. 1b). This novel in-situ evolutionary oxide-anion dual-layer mechanism greatly extends the corrosion resistance of the electrode in harsh seawater environment.

## 2. Experimental section

### 2.1. Pre-activation of melamine sponge

The melamine sponge (MS) used in this study requires no pretreatment prior to use. MS was cut into small pieces measuring  $25 \times 25 \times 2 \text{ mm}$ . In a beaker, a specific amount of  $\text{AgNO}_3$  ( $5 \text{ g L}^{-1}$ ) was taken and  $\text{NH}_3\cdot\text{H}_2\text{O}$  ( $2.6 \text{ mL L}^{-1}$ ) was added drop by drop with continuous shaking. The  $\text{AgNO}_3$  solution gradually turned turbid. The addition of  $\text{NH}_3\cdot\text{H}_2\text{O}$  continued until the turbid solution cleared. Next, a certain amount of glucose ( $\text{C}_6\text{H}_{12}\text{O}_6$ ,  $8 \text{ g L}^{-1}$ ) was added while vigorously shaking to thoroughly mix the solution. The cut MS pieces were then immersed in the prepared solution. The test tube containing the sponge and solution was placed in a water bath and maintained at room temperature for a specific duration. Upon completion of the silver mirror reaction, the sponge foam was carefully removed and rinsed with distilled water.

### 2.2. Preparation of Ni-Fe-Ce-B/MS electrode

To prepare Ni-Fe-Ce-B/MS electrode, ammonium ceric sulfate ( $(\text{NH}_4)_4\text{Ce}(\text{SO}_4)_4\cdot 4 \text{ H}_2\text{O}$ , 0.05 g), potassium sodium tartrate ( $\text{NaK-C}_4\text{H}_4\text{O}_6\cdot 4 \text{ H}_2\text{O}$ , 4.23 g), ammonium iron (II) sulfate ( $\text{Fe}(\text{NH}_4)_2(\text{SO}_4)_2\cdot 6 \text{ H}_2\text{O}$ , 1.18 g), sodium citrate ( $\text{C}_6\text{H}_5\text{Na}_3\text{O}_7\cdot 3 \text{ H}_2\text{O}$ , 3.12 g) and nickel sulfate ( $\text{NiSO}_4\cdot 6 \text{ H}_2\text{O}$ , 1.82 g) was dissolved in 100 mL water, followed by the addition of dimethylamine borane (0.36 g) into the solution. Adjust pH = 10 with  $\text{NH}_3\cdot\text{H}_2\text{O}$ . The pretreated melamine sponge was submerged in the plating solution for a duration of 240 min at a temperature of  $80^\circ\text{C}$ . After electroless plating, the as-prepared Ni-Fe-Ce-B/MS electrode was washed by deionized water and stored in ethanol.

### 2.3. Characterization

Scanning electron microscopic (SEM) measurements were conducted using a Hitachi SU-70 microscope. Transmission electron microscope

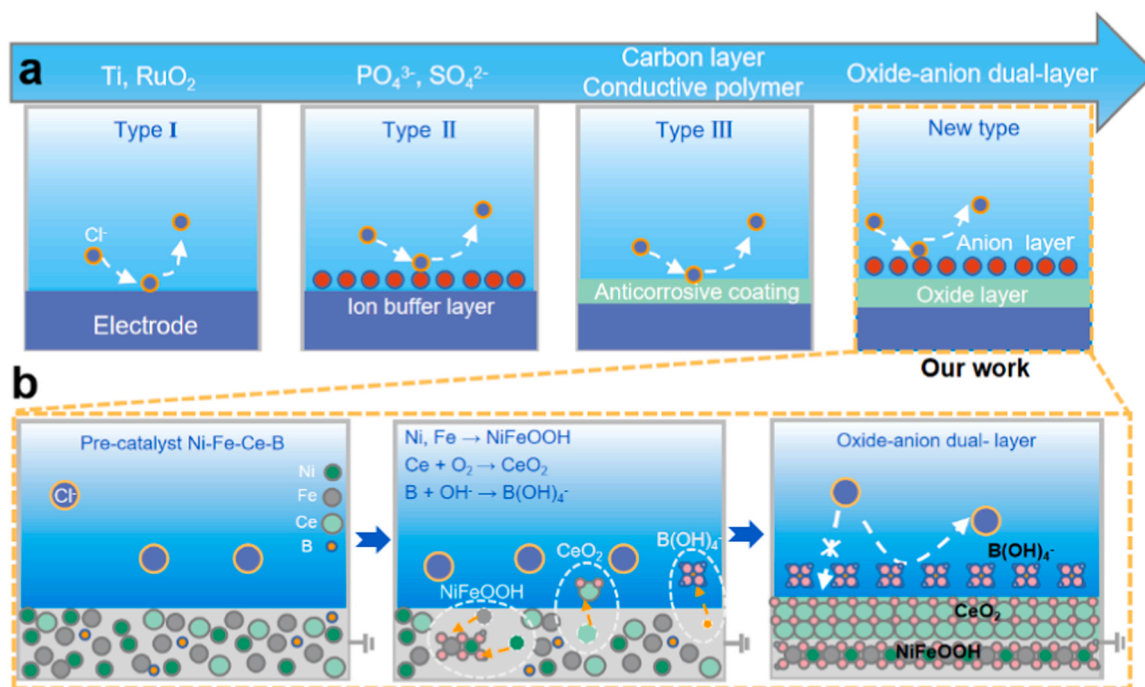


**Fig. 1.** Novel anti-corrosion mechanism. (a) Schematic of anti-corrosion electrode types for seawater electrocatalysis: (Type I) Electrode with inherent-corrosion-resistance, (Type II) Electrode with ion buffer layer, (Type III) Electrode with anticorrosive coating and (Type IV) Electrode with oxide-anion dual-layer (our work). (b) The in-situ evolutionary formation process of  $\text{CeO}_2\text{-B}(\text{OH})_4^-$  dual-layer during OER.

(TEM) measurements were performed on a FEI Talos F200x. Characterization through X-ray diffraction (XRD) took place utilizing a state-of-the-art Bruker D8-Advance instrument, armed with Cu K $\alpha$  radiation to generate the required analytical information. Inductively coupled plasma-atomic emission spectroscopy (ICP-AES) analysis was measured on Model ARCOS FHS12 instrument. Energy Dispersive X-ray (EDX) spectroscopy measurements were meticulously conducted using an ESCALABMK II system, with magnesium serving as the excitation source to accurately acquire spectral data. Raman spectra were carried out by a LabRAM HR Evolution. In-situ Raman spectroscopy was performed using the Renishaw inVia Raman Microscope with a 532 nm laser excitation, while subjecting the sample to a range of precisely controlled potentials through an electrochemical workstation. X-ray photoelectron spectroscopy (XPS) was conducted on PerkinElmer PHI 5000 C. Time of Flight Secondary Ion Mass Spectrometry (TOF-SIMS) was conducted on PHI Nano TOF II.

#### 2.4. Electrochemical measurements

Electrochemical measurements were performed using a CHI 760E electrochemical workstation. A three-electrode cell system was employed, consisting of a mercuric oxide electrode as the reference electrode, a carbon rod as the counter-electrode, and the prepared electrodes as the working electrodes. Before initiating the hydrogen evolution reaction (HER) and OER, the system was thoroughly purged with high-purity anhydrous nitrogen (N<sub>2</sub>) and oxygen (O<sub>2</sub>) gases, respectively, ensuring an inert atmosphere for 30 min to optimize conditions for the reactions. Linear sweep voltammetry (LSV) measurements were conducted in electrolyte at a scan rate of 5 mV s<sup>-1</sup>. The tested potential vs Hg/HgO can be converted into potential with respect to the reversible hydrogen electrode (RHE) via the Nernst equation listed as follows:

$$E(\text{RHE}) = E(\text{Hg/HgO}) + 0.0977 \text{ V} + 0.0596 \text{ pH}$$

Electrochemical impedance spectroscopy (EIS) were recorded at the potential of 10 mA cm<sup>-2</sup>, with a frequency range from 10<sup>-1</sup> to 10<sup>5</sup> Hz. In polarization tests (three electrode system) mentioned in the paper, the compensation rate is 85 %.

#### 2.5. Free energy for HER process

*Materials Studio* was used to simulate the hydrogen adsorption free energy of different sample to evaluate the HER activity. Perdew Burke Ernzerhoff (PBE) functional under the pseudopotential plane wave method and generalized gradient approximation (GGA) is used. In simulation process, Fe-B, Ni-B, Ni-Ce-B, Ni-Fe-B, Ni-Fe-Ce-B amorphous models by amorphous cell are established, and 15 Å vacuum layers are established along the z-axis. The thickness of the amorphous model atomic layer is 4 layers. The atoms and adsorbed atoms in the top two layers underwent full relaxation, while the atoms in the lower two layers were held fixed. To account for strong electron correlation effects, several important corrections were incorporated, including the on-site Hubbard corrections and dispersion correction. The specific values used for the on-site Hubbard correction, denoted as  $U_{\text{eff}}$ , were 5.5 eV for Ni, 5 eV for Fe, and 4.5 eV for Ce. The  $k$ -point sampling in the Brillouin zone is carried out using the Monkhorst-Pack automatic generation method, and the plane wave truncation energy is set at 440 eV. To minimize the system energy, geometry optimization is carried out under the above conditions.

#### 2.6. Free energy for OER process

The projected augmented wave potentials were selected to represent the ionic cores, utilizing a plane wave basis set with a kinetic energy cutoff of 400 eV. Geometry optimizations were conducted with force

convergence set below 0.05 eV/Å, and the electronic energy was considered self-consistent when the energy change was less than 10<sup>-5</sup> eV. The  $\Gamma$ -centered (2 × 2 × 1) Monkhorst-Pack  $k$ -point grids were used for calculation. All the atoms are relaxed in all the calculations.

#### 2.7. Molecular dynamic simulations

Molecular dynamic (MD) simulations (*Materials Studio*) were performed to study the anion distributions close to the electrode surface. A 5 Å thick layer of Ni was positioned at the base of the container and secured as the representative model for the electrode surface. To simulate the electrolyte in the experiment, the solvent model contains 2102 water molecules, 153 K<sup>+</sup>, 63 Na<sup>+</sup>, 26 B(OH)<sub>4</sub><sup>-</sup>, 127 OH<sup>-</sup> and 63 Cl<sup>-</sup>, corresponding to the density of 1.1 g cm<sup>-3</sup>. The Berendsen thermostat was utilized within the canonical (NVT) ensemble. Initially, the systems were heated from 300 to 500 K with 20 K ps<sup>-1</sup>, then equilibrated at 500 K for 10 ps to fully relax the configuration. Finally, the solution was cooled to 298 K for 2 ns to collect data. An electric field of 1 V/Å in the Z direction was applied to each atom. The cutoff of Coulomb and Lennard-Jones interaction was 10 Å, and time step was 2 fs.

### 3. Results and discussion

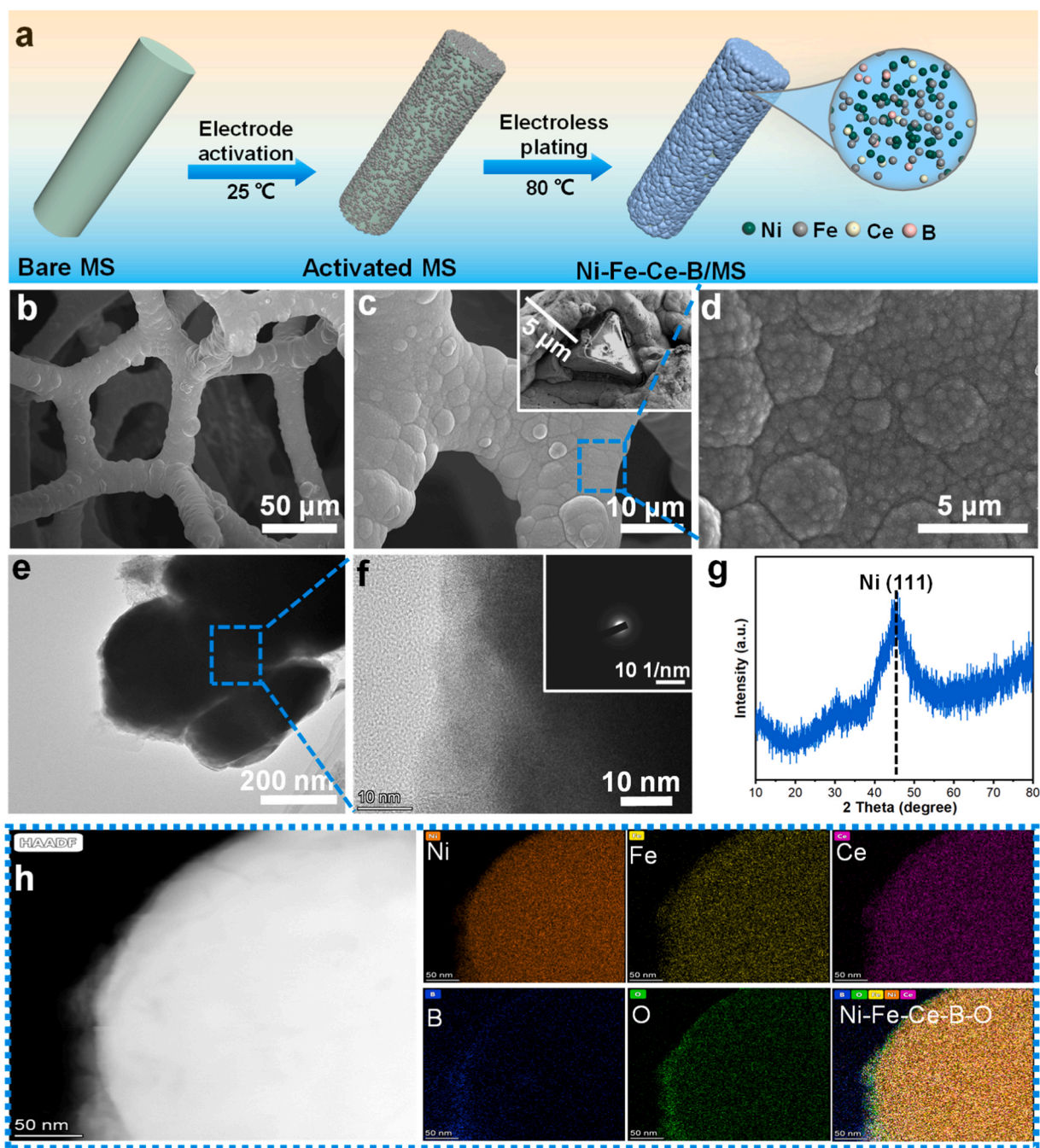
#### 3.1. Synthesis and structure characterizations of Ni-Fe-Ce-B/MS electrode

Fig. 2a describes the stepwise fabrication of Ni-Fe-Ce-B/MS electrode. Ag@MS was first synthesized, then coated with Ni-Fe-Ce-B via a simple electroless plating method under mild condition [20]. Synthesis details are provided in the [supplementary material](#).

After the preparation of Ni-Fe-Ce-B/MS electrode, we initially assessed its surface morphology using a SEM. The developed Ni-Fe-Ce-B/MS electrode exhibits a three dimensional (3D) continuous structure that closely resembles the original shape of the MS (Fig. 2b, c; and Fig. S1), with a maximal thickness of the catalytic layer reaching up to ~ 5 μm (insert SEM image in Fig. 2c). Its surface displays a characteristic multi-level cellular micro-nano structure formed via electroless plating with well-defined geometrical features (Fig. 2d), providing an extensive surface area along with a substantial quantity of active sites, contributes to highly efficient catalytic activity. TEM image shows that the diameter of small catalyst particles formed by electroless plating is 50–500 nm (Fig. 2e). No obvious lattice structure is found in the high magnification TEM image and typical amorphous diffraction ring is shown in the insert selected area electron diffraction (SAED) pattern (Fig. 2f), indicating that Ni-Fe-Ce-B obtained by electroless plating at low temperature is of an amorphous state. Furthermore, XRD result without obvious sharp peak also verifies the prepared electrode is amorphous (Fig. 2g). The failure of crystal growth at low temperatures results in the formation of amorphous phases in the crystal nucleus due to insufficient time for crystal nuclei to form and develop. Furthermore, the high-angle annular dark field STEM-EDX (HAADF-STEM-EDX) and SEM-EDX images (Fig. 2h; and Fig. S2) both suggest a uniform distribution of Ni, Fe, Ce, B and O elements on the surface of electrode. Furthermore, the concentration of oxygen in the surrounding region of the catalyst is notably higher than that at the inner core of the catalyst (Fig. 2h). That is due to the Ni-Fe-Ce-B electrocatalyst has a propensity to form an oxide layer on its surface even when exposed to ambient air. The elemental ratio of Ni: Fe: Ce: B was further ascertained to be 1: 0.79: 0.05: 0.25 by ICP-AES analysis (Table S1), outlining the composition of the Ni-Fe-Ce-B catalyst. Noteworthy is the measured density of these electrodes, recorded at ~ 0.24 g cm<sup>-3</sup> (Table S2), closely resembling that of commercial nickel foam.

In an experiment to test the storage stability of different comparison samples in oxygen-saturated deionized water for a week, the Ni-B/MS electrode without Fe did not show any apparent change (Fig. S3), whereas the Fe-B and Ni-Fe-B/MS electrodes exhibited rust formation,





**Fig. 2.** Preparation procedure, morphological and structural analysis of pre-electrode. (a) Schematic of the preparation process. (b–d) SEM images (Insert in 2c shows SEM image of the cross-section of electrode). (e, f) TEM images (Insert in 2f shows the SAED pattern). (g) XRD pattern, and (h) HAADFSTEM image & HAADFSTEM-EDX images of Ni-Fe-Ce-B/MS electrode.

damaging their cellular structures, as confirmed by Fig. S4. However, despite containing Fe, the Ni-Fe-Ce-B/MS electrode maintained its form, indicating no visible oxidation. This could be due to the added Ce element which possibly forms a dense oxide layer, hindering O<sub>2</sub> and electron transmission and slowing down surface corrosion, thereby enhancing stability of the electrode [21].

### 3.2. Electrochemical performance

HER performance of Ni-Fe-Ce-B was measured in 1 M KOH + 0.5 M NaCl using a standard three-electrode electrochemical cell. Fig. 3a shows the LSV curves of Pt/C/NF, Fe-B, Ni-B, Ni-Fe-B, Ni-Ce-B and Ni-Fe-Ce-B/MS electrode. The Ni-B/MS electrode requires overpotentials ( $\eta$ ) of

only 65 and 134 mV to reach 10 and 50 mA cm<sup>-2</sup>, which closely resemble those of Pt/C ( $\eta_{10}$  = 63 mV,  $\eta_{50}$  = 126 mV,  $\eta_{10}$  represents the overpotential of the electrode at a current density of 10 mA cm<sup>-2</sup>) (Table S3). With the introduction of Ce or Fe, Ni-Ce-B ( $\eta_{10}$  = 57 mV,  $\eta_{50}$  = 145 mV) and Ni-Fe-B/MS electrode ( $\eta_{10}$  = 43 mV,  $\eta_{50}$  = 119 mV) exhibit more excellent HER performance. Moreover, Ni-Fe-Ce-B/MS electrode enjoys an exceptional HER catalytic capacity, achieving 10 and 50 mA cm<sup>-2</sup> at only 40 and 101 mV, respectively, superior to those of Ni-Ce-B and Ni-Fe-B/MS electrodes. A smaller Tafel slope signifies a more rapid kinetic process, implying that the catalyst can attain the necessary current with a reduced overpotential. From Fig. 3b, Tafel slope of Ni-Fe-Ce-B/MS electrode is only 31 mV dec<sup>-1</sup>, which is obviously the smallest one among the electrodes. The suggestion is that the



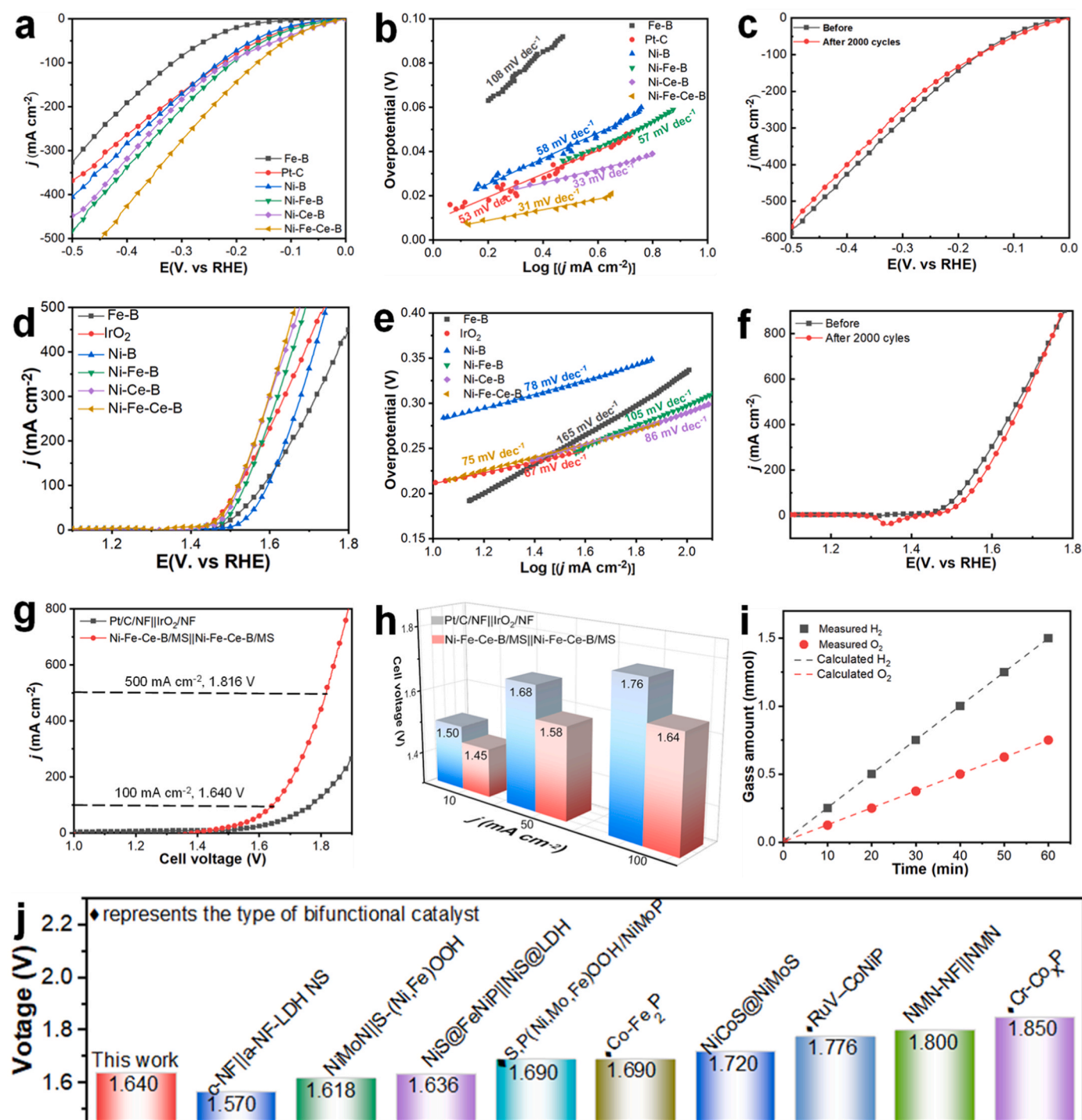


**Fig. 3.** Electrochemical performance. *iR*-corrected LSV curves (a) and Tafel plots (b) of Pt-C/NF, Fe-B, Ni-B, Ni-Fe-B, Ni-Ce-B and Ni-Fe-Ce-B/MS electrode toward HER in 1 M KOH + 0.5 M NaCl. (c) Comparison of HER curves of Ni-Fe-Ce-B/MS electrode before and after 2000 cycles. *iR*-corrected LSV curves (d) and Tafel plots (e) for IrO<sub>2</sub>/NF, Fe-B, Ni-B, Ni-Fe-B, Ni-Ce-B and Ni-Fe-Ce-B/MS electrode for OER in 1 M KOH + 0.5 M NaCl. (f) Comparison of OER curves of Ni-Fe-Ce-B/MS electrode before and after 2000 cycles. (g) Polarization curves for water electrolysis using various electrode couples in 1 M KOH + 0.5 M NaCl. (h) Bar chart of voltage comparison between different electrode couples under 10, 50 and 100 mA cm<sup>-2</sup>. (i) Comparison between the actual and theoretical yields of gaseous products from the two-electrode electrolyzer was conducted under a constant current density of 100 mA cm<sup>-2</sup> in a solution of 1 M KOH + 0.5 M NaCl. (j) Comparison of the cell voltage at the current density of 100 mA cm<sup>-2</sup> of different electrode couples in previous literatures to drive water electrolysis in 1 M KOH + 0.5 M NaCl.

HER is taking place through the Volmer mechanism, where the rate-determining step (RDS) is the electrochemical desorption. After 2000 cycles, the HER performance of Ni-Fe-Ce-B sample slightly declined, preliminarily indicating that it has excellent electrochemical stability in alkaline simulated seawater (Fig. 3c). EIS Nyquist plots in Fig. S5 further indicate that Ni-Fe-Ce-B/MS electrode has more favorable charge-

transfer resistance ( $R_{ct}$ , 1.2  $\Omega$ ) in comparison with Pt/C/NF (NF stands for nickel foam) ( $R_{ct}$ , 20.6  $\Omega$ ), Fe-B ( $R_{ct}$ , 7.1  $\Omega$ ), Ni-B ( $R_{ct}$ , 4.8  $\Omega$ ), Ni-Fe-B ( $R_{ct}$ , 2.5  $\Omega$ ) and Ni-Ce-B/MS electrode ( $R_{ct}$ , 2.4  $\Omega$ ), demonstrating its efficient charge-transport capability and favorable HER dynamics. Another insightful approach to measuring double-layer capacitances ( $C_{dl}$ ) is utilized in this context.  $C_{dl}$  is directly proportional to the

electrochemical surface area (ECSA), enabling a meaningful relative comparison. Obtained from the cyclic voltammograms versus the scan rate in 1.0 M KOH + 0.5 M NaCl, the  $C_{dl}$  of 55.1 mF cm<sup>-2</sup> on Ni-Fe-Ce-B/MS electrode is the highest as compared to the benchmark Pt/C/NF (10.1 mF cm<sup>-2</sup>), Fe-B (20.1 mF cm<sup>-2</sup>), Ni-B (22.2 mF cm<sup>-2</sup>), Ni-Fe-B (51.1 mF cm<sup>-2</sup>) and Ni-Ce-B/MS electrode (48.2 mF cm<sup>-2</sup>), as shown in Figs. S6 and S7. The highest  $C_{dl}$  value implies the enriched active sites on Ni-Fe-Ce-B/MS electrode surface for HER.

Fig. 3d illustrates the OER activity of the electrodes using various catalysts in 1.0 M O<sub>2</sub>-saturated KOH + 0.5 M NaCl. The Ni-Fe-Ce-B/MS electrode exhibits the best OER performance with only 208 mV for reaching 10 mA cm<sup>-2</sup>, lower than 214 mV for benchmark IrO<sub>2</sub>/NF, 257 mV for Fe-B, 261 mV for Ni-B, 222 mV for Ni-Fe-B, and 230 mV for Ni-Ce-B/MS electrode. As is well known, in the anodic reaction region of seawater electrocatalysis, OER and ClER are a pair of competitive reactions relating to potential and pH value. Previous studies have shown that in alkaline environments with pH of 14, low overpotential ( $\eta < 480$  mV) can inhibit the occurrence of ClER (Fig. S8) [22]. Due to the relatively high activity of OER catalysts in alkaline solutions, the occurrence of ClER can usually be avoided. At 50, 100 and 500 mA cm<sup>-2</sup>, the overpotentials of the Ni-Fe-Ce-B/MS electrode are 269, 297 and 434 mV, respectively, less than 480 mV, indicating that the electrode is suitable for industrial application scenarios under large current density. A Tafel slope of 75 mV dec<sup>-1</sup> is obtained for the Ni-Fe-Ce-B, which is more favorable than those of Fe-B (165 mV dec<sup>-1</sup>) (Fig. 3e), Ni-B (78 mV dec<sup>-1</sup>), Ni-Fe-B (105 mV dec<sup>-1</sup>) and Ni-Ce-B/MS electrode (86 mV dec<sup>-1</sup>), while close to that of IrO<sub>2</sub>/NF electrode (67 mV dec<sup>-1</sup>). Moreover, the OER performance of the Ni-Fe-Ce-B sample after 2000 cycles slightly weakened (Fig. 3f). The decrease in performance is potentially related to the inevitable chloride ion corrosion. No light green stimulating gas was found, indicating that ClER was inhibited. Furthermore, the lowest  $R_{ct}$  of only 0.7  $\Omega$  (Fig. S9) with higher ECSA of 42.0 mF cm<sup>-2</sup> (Fig. S10, S11), respectively, for the Ni-Fe-Ce-B/MS electrode compared to IrO<sub>2</sub>/NF ( $R_{ct}$ , 15.2  $\Omega$ ;  $C_{dl}$ , 2.26 mF cm<sup>-2</sup>), Fe-B ( $R_{ct}$ , 2.5  $\Omega$ ;  $C_{dl}$ , 26.2 mF cm<sup>-2</sup>), Ni-B ( $R_{ct}$ , 1.4  $\Omega$ ;  $C_{dl}$ , 34.1 mF cm<sup>-2</sup>), Ni-Fe-B ( $R_{ct}$ , 1.9  $\Omega$ ;  $C_{dl}$ , 39.4 mF cm<sup>-2</sup>), and Ni-Ce-B/MS electrode ( $R_{ct}$ , 1.1  $\Omega$ ;  $C_{dl}$ , 38.0 mF cm<sup>-2</sup>), indicating the superior intrinsic conductivity and high density of active sites for the former contribute to the fastest electron-transfer kinetics, synergistically enhancing the OER activity.

Encouraged by the exceptional performance observed in HER and OER, the overall simulated seawater splitting performances were measured using the Ni-Fe-Ce-B/MS as a bifunctional electrode and a control group of Pt/C-IrO<sub>2</sub> couple. As shown in Fig. 3g, the Ni-Fe-Ce-B/MS || Ni-Fe-Ce-B/MS system only needs a low cell voltage of 1.451, 1.580, and 1.640 V to deliver 10, 50 and 100 mA cm<sup>-2</sup>, respectively, whereas 1.502, 1.681 and 1.760 V are required in the case of Pt/C on NF || IrO<sub>2</sub> on NF couple (Fig. 3h), suggesting a significantly superior performance in the context of simulated seawater electrolysis. Even under the larger current density of 0.5 A cm<sup>-2</sup>, the Ni-Fe-Ce-B/MS || Ni-Fe-Ce-B/MS system needs only 1.816 V. Faradic efficiency (FE) was quantified using the water drainage method with an assembled electrolyzer. The corresponding result indicates an almost 100 % FE on our catalyst for the simulated seawater electrolysis (Fig. 3i). This demonstration underscores that the primary source of current density arises from the electrolysis of seawater. It has come to attention that the overall water splitting performance of the Ni-Fe-Ce-B/MS || Ni-Fe-Ce-B/MS system surpasses that of most previously studied electrode couples (Fig. 3j; and Table S4) [13,23–30], let alone its outstanding stability preventing chloride ion corrosion.

### 3.3. Origin of electrocatalytic activity

To investigate the evolution of the Ni-Fe-Ce-B/MS electrode during the processes of HER and OER, XPS measurements were conducted to analyze the chemical states of surface elements before and after 24-h

durability experiments corresponding to each reaction. In the pristine Ni-Fe-Ce-B sample, the existence of elemental Ni, Fe, Ce, and B was identified (Fig. S12). Moreover, the Ni 2p 3/2 and Fe 2p 3/2 level was negatively shifted by 0.3 and 3.1 eV relative to that of metallic Ni<sup>0</sup> (852.1 eV) and metallic Fe<sup>0</sup> (709.4 eV). [31] In contrast, B 1s and Ce 3d 5/2 level exhibited positive shifts of 0.3 and 0.5 eV, respectively, compared to that these of elemental boron (187.1 eV) and metallic Ce (883.9 eV). [32] These findings imply the presence of a Ni-Fe-Ce-B alloy within the prepared catalyst. B and Ce act as electron donors to Ni and Fe, which results in an increase in their electron density.

After 24 h of HER, peak intensity corresponding to Ni<sup>0</sup> increased, and Ni on the catalyst surface was predominantly observed in the Ni (II) oxidation state. These findings suggest that surface reduction and formation of the Ni(OH)<sub>2</sub> (Fig. S13a) also occur during the HER. [20] The binding energies of elements like Ni, Fe, Ce, and B across various valence states exhibit a shift towards the positive direction. This phenomenon is primarily attributed to the reducing influence of the hydrogen environment. DFT calculation was further performed to give insight into the outstanding HER performance of these metal boride. Free energy profile of HER process was depicted in Fig. S14. The hydrogen binding energy ( $\Delta G_{H^*}$ ) close to zero was corresponding to the electrocatalyst with high activity. The Fe-B and Ni-B show  $|\Delta G_{H^*}|$  values of 0.565 and 0.508 eV, respectively. With the incorporation of Ni and Ce,  $\Delta G_{H^*}$  of Ni-Fe-B ( $|\Delta G_{H^*}| = 0.460$  eV) and Ni-Ce-B ( $|\Delta G_{H^*}| = 0.479$  eV) can be further optimized. Ni-Fe-Ce-B has the most efficient  $\Delta G_{H^*}$  (−0.433 eV) among those of the control samples. These theoretical calculation results are consistent with the experimental results. Fe and Ce might alter the d-band center position of Ni sites, thus optimizing the hydrogen adsorption free energy.

After 24 h of performing the OER, it was observed that the peaks corresponding to the elemental forms of Ni, Fe, Ce, and B on the pristine electrode had disappeared, indicating the prevalence of their oxidized states (Fig. S12). The intensity of the B peak has noticeably decreased, likely attributed to the leaching of surface elements into the electrolyte, resulting in the generation of borate anions. Furthermore, the O 1s spectra reveal a transition in binding energy for surface-dominated adsorbed oxygen species, shifting from 531.4 eV for Ni(OH)<sub>2</sub> to 530.6 eV for NiOOH [33]. The same evolution applies to the Fe element, which exists in the form of higher valence of FeOOH. From SEM image (Fig. S13b), after undergoing the OER reaction, the outer layer of the catalyst particles is wrapped in an amorphous NiFeOOH [34]. The oxidation state of Ce is more obvious, which mainly exists in the form of oxides. Ce element is more easily oxidized than Ni and Fe element at room temperature, and forms oxides when exposed to air. As illustrated in the inset in Fig. 4a, the lattice distance of 0.270 nm can be ascribed to (100) crystalline facet of CeO<sub>2</sub>. CeO<sub>2</sub> is uniformly distributed on the surface of the catalyst, thereby slowing down the oxidation of Ni and Fe. Moreover, the surface of the catalytic electrode changed from an amorphous state to dispersed CeO<sub>2</sub> crystal particles. This is because under the atmosphere of oxygen, Ce elements are preferentially converted into oxides and distributed on the surface of the catalytic electrode [35].

In-situ Raman spectroscopy is utilized to observe and track the reconstruction process of the pre-catalyst Ni-Fe-Ce-B during OER. As can be seen in Fig. 4b and c, when the potential is raised to 1.35 V, two distinct peaks become clearly evident at approximately 324 and 523 cm<sup>-1</sup>. These two peaks are indicative of the vibrations associated with Ni-OH and Ni-O, thereby signifying the formation of Ni(OH)<sub>2</sub> [36]. Upon further raising the potential to approximately 1.45 V, these two peaks undergo a shift to 477 and 550 cm<sup>-1</sup>, corresponding to the bending vibration of  $E_g$  ( $\delta$ (Ni-O)) and tensile vibration of  $A_{1g}$  ( $\nu$ (Ni-O)) of NiOOH, respectively [37]. The high ratio of  $\delta$ (Ni-O) to  $\nu$ (Ni-O) suggests the formation of  $\gamma$ -NiOOH. The peak at 720 cm<sup>-1</sup> is a characteristic peak of  $\gamma$ -FeOOH species [38]. The highly oxidized nickel and iron species are commonly thought to exist in the form of  $\gamma$ -NiFeOOH, characterized by a more disordered structure, and are known to offer



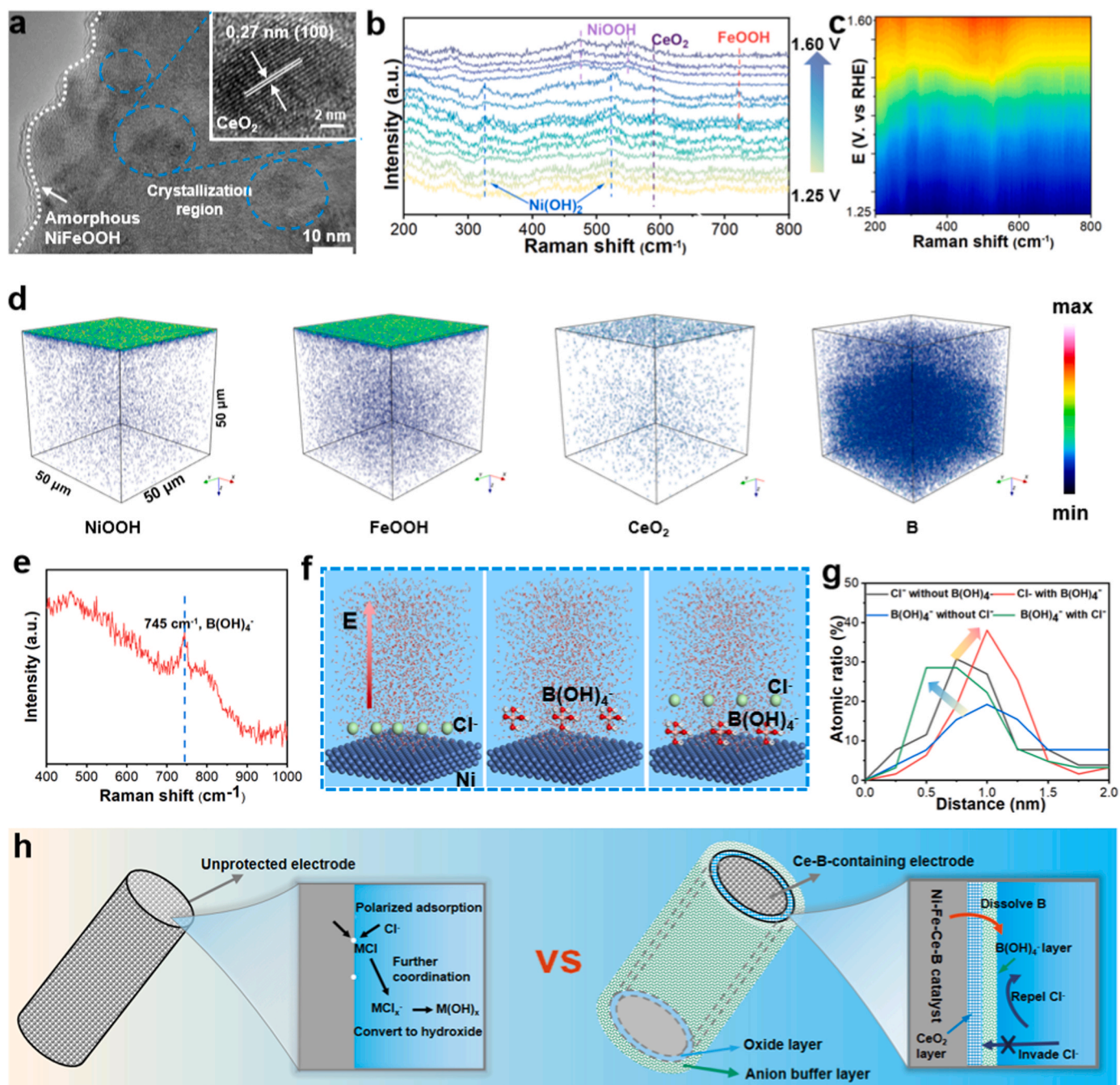


**Fig. 4.** Characterization of dual-layer and origin of corrosion resistance. (a) TEM images of Ni-Fe-Ce-B catalyst after 24-h OER (Inset shows TEM image of CeO<sub>2</sub> lattice structure). (b) and (c) In-situ Raman spectra of Ni-Fe-Ce-B/MS electrode for OER at different voltage (1.25–1.60 vs RHE). (d) TOF-SIMS images of spatial distribution of different components. (e) Raman spectrum of the electrolyte after OER. (f) Schematic of the distribution of different ions in the solution under an electric field. (g) The radial distribution of Cl<sup>-</sup> and B(OH)<sub>4</sub><sup>-</sup> anions in different systems. (h) Schematic diagram of unprotected electrodes corroded by chloride ions (left) and the prepared electrode structure with oxide-anion dual-layer in seawater (right).

increased OER activity. As the voltage increases, the peak values of CeO<sub>2</sub> and FeOOH decrease, which may be due to the influence of bubbles generated on the electrode surface on signal collection. The high valence Ni generated during the OER is a truly active species. The presence of Fe and Ce alters the redox properties of Ni, thus causing the potential of  $\gamma$ -NiOOH to shift forward, increasing the average oxidation state of Ni and enhancing its activity in catalytic reactions (Fig. S15) [39,40].

To gain a profound understanding of the enhancements in OER performance resulting from the incorporation of CeO<sub>2</sub> and Fe, and to specifically elucidate the nature of active sites, we conducted DFT calculations. These calculations enabled a comparative investigation of the

elementary steps involved in the four-electron OER process over four catalysts: CeO<sub>2</sub>, NiOOH, NiFeOOH, and CeO<sub>2</sub> @NiFeOOH (Fig. S16). The assessment of catalytic activity heavily relies on determining the crucial parameter of the limiting reaction barrier, derived from the RDS in the context of free energy. From Fig. S17, CeO<sub>2</sub> in its bare form is typically considered a subpar OER catalyst, as it exhibits a notably high energy barrier of approximately 2.45 eV for the initial step of the reaction. The RDS for NiOOH was identified as the formation of \*OOH, with the corresponding  $\Delta G$  being as high as 1.96 eV. This implies that a significant bottleneck in the process arises from the unfavorable bindings between \*O and \*OOH species. The RDS for OER of NiFeOOH is the



second step from  $^*\text{OH}$  to  $^*\text{O}$ , revealing a more efficient OER kinetic than that of  $\text{NiOOH}$  ( $\Delta G_{^*\text{OH} \rightarrow ^*\text{O}} = 1.94 \text{ eV}$ ). For  $\text{NiFeOOH}$  system, the surface fast spin high valent Fe site delivers the O radical more easily, while it is still the surface closed shell high valent Ni site that better catalyzes the O-O coupling. Thus, it is the synergy between Fe and Ni that offers the optimal performance of  $\text{NiFeOOH}$  for catalyzing OER. The introduction of Fe element is beneficial for promoting M-O binding in the OER process. The free energy diagram at 1.23 V demonstrates that  $\text{CeO}_2/\text{NiFeOOH}$  exhibits the lowest  $\Delta G_{\text{OH}^*}$ , signifying an improved  $\text{OH}^*$  adsorption. Furthermore, the RDS for  $\text{CeO}_2/\text{NiFeOOH}$  involves the conversion of  $\text{OH}^*$  into  $\text{O}^*$  with a limiting energy barrier of 0.64 eV, which is lower than the barriers for both  $\text{NiFeOOH}$  (0.76 eV) and  $\text{NiOOH}$  (0.70 eV). This suggests that  $\text{O}^*$  can readily adsorb onto the surface of  $\text{CeO}_2/\text{NiFeOOH}$ . The intimate interaction between  $\text{CeO}_2$  and  $\text{NiFeOOH}$  species likely establishes a d-f electron ladder, facilitating the rapid transfer of electrons across the catalytic surface [41]. At the same time, Ce promotes the formation of superoxide or the release of oxygen, and Ce doping can effectively optimize the energy levels of OER intermediates [42].

### 3.4. Origin of corrosion resistance of Ce-B containing electrode

Tafel polarization test can characterize the corrosion resistance of coating materials. To preliminarily verify the anti-corrosion effect of Ce and B elements in seawater electrocatalysis, we conducted a set of controlled cyclic experiments. In 1 M KOH + 0.5 M NaCl, Ni-Fe-Ce-B/MS electrode exhibits the highest polarization potential and excellent polarization current density (Fig. S18), indicating that Ni-Fe-Ce-B/MS electrode can stably exist in more demanding seawater environments. In Fig. S19, when the electrochemical reaction is in progress in the presence of a Ni-Fe alloy electrode, the applied voltage experiences a rapid decrease within 3000 s. This result is accompanied by the significant deposition of black solid powders on the electrode surface. (Fig. S20a). It indicates that the commercial Ni-Fe foam electrode is corroded seriously in simulated seawater. After 5000 s of stability test, the performance of the Ni-Fe-B/MS electrode also decreased by  $\sim 40\%$ . By contrast, the Ni-Fe-Ce-B/MS electrode can electrocatalyze OER stably for 5000 s, with the almost unchanged electrode appearance (Fig. S20b). These preliminary results indicate that Ce and B elements have played a significant role in improving corrosion resistance.

TOF-SIMS images can visually display the elemental composition and distribution on the surface and inside of the electrode (Fig. 4d). Upon conducting a 24-h OER testing, it was observed that the elements Fe and Ni had transformed into  $\text{NiFeOOH}$ , manifesting a layer thickness of approximately 10–20 nanometers. Concurrently, the Ce element was present on the surface in the form of an oxide layer, measuring around 5–10 nanometers in thickness. This signifies that  $\text{CeO}_2$  is situated on the outermost stratum of the catalytic electrode. Additionally, the surface concentration of the B element was notably lower than its interior, suggesting a loss of boron from the electrode. After long term 48-h stability test for OER in 1 M KOH + 0.5 M NaCl, the pH value of alkaline simulated seawater remained consistently stable, and the dissolved concentrations of Ni, Fe, and Ce in alkaline simulated seawater were consistently below 0.1 ppm (Table S5). This underscores the robust compositional stability of the surface catalyst during prolonged operation in alkaline simulated seawater. The rationale lies in the ability of these metallic elements to establish stable compounds such as  $\text{Ni}(\text{OH})_2$  and  $\text{NiFeOOH}$ . And they are also shielded by  $\text{CeO}_2$  coatings, subsequently reducing their propensity to dissolve and diffuse into the electrolyte. Unlike metal elements, the presence of B was detected by ICP in the electrolyte after water electrolysis. As electrolysis progresses, element B dissolves and diffuses into alkaline electrolyte (Fig. S21), which is consistent with the results of TOF-SIMS. Noteworthy, for B in the original sample, the valence bond form of B is very rich. For example, B can form B-B or B-M bond, [43] so it also tends to produce a variety of transformations during the electrochemical process in alkaline

solution. When electrocatalysis is in progress, metal boride might convert into metal borate [44], while isolated B element in the electrode eventually precipitates into the solution to form metaborate anions ( $\text{BO}_2^-$ ), and then mainly converted to  $\text{B}(\text{OH})_4^-$  under alkaline condition. The peak presents at  $745 \text{ cm}^{-1}$  from Raman spectrum confirms the existence of  $\text{B}(\text{OH})_4^-$  (Fig. 4e) [45]. The local electrolyte microenvironment can affect the adsorption behavior of  $\text{Cl}^-$  on the electrode surface. Studies have confirmed that oxyacid radicals such as  $\text{PO}_4^{3-}$  [8],  $\text{SO}_4^{2-}$  [9], exhibit a preference for adsorption on the surface of anode, leading to the formation of a negatively charged layer. This layer, in turn, generates electrostatic repulsion, effectively pushing chloride ions away from the anode. Similarly, it is noticed that  $\text{B}(\text{OH})_4^-$  and  $\text{Cl}^-$  have the same negative charge, so  $\text{B}(\text{OH})_4^-$  has a natural repulsive force with  $\text{Cl}^-$ . Increasing the distance between  $\text{Cl}^-$  and the electrode surface can prevent the occurrence of the corrosion reactions. By simulating the diffusion of ions under an electric field, when only  $\text{Cl}^-$  or  $\text{B}(\text{OH})_4^-$  exists in an alkaline solution, most of  $\text{Cl}^-$  and  $\text{B}(\text{OH})_4^-$  aggregated at distances of 0.75 and 1 nm from the Ni electrode, respectively. However, when the two ions coexist, borate anions ( $\text{B}(\text{OH})_4^-$ ) tend to reside in the inner Helmholtz layer closer to the electrode surface, whereas chloride anions are located further outside (Fig. 4f, g). The hierarchical anions could reduce the probability of chloride ion corrosion [37].

Under the action of an electric field,  $\text{Cl}^-$  approaching the unprotected electrode surface will cause a series of corrosion reactions (Fig. 4h). Fortunately, the above experiments and theoretical calculation mentioned that there were some changes in the structure of the interface of electrode-electrolyte during seawater electrooxidation. Therefore, we speculate that during the electrocatalytic process, the coordination of  $\text{CeO}_2$  coated on the outer layer of the inner electrode and  $\text{B}(\text{OH})_4^-$  anions aggregated at the electrolyte-electrode interface invades and repels the attack of chloride ions (Fig. 4h). It is worth noting that although the amount of dissolved B is relatively small, the  $\text{B}(\text{OH})_4^-$  formed by them will fill the inner Helmholtz layer, forming a very thin layer of “armor”.

Further understanding is needed on the impact of oxide layer strategy and ion layer strategy on OER performance. From Fig. S22a, some comparison experiments were performed to further examine the roles for  $\text{CeO}_2$  and  $\text{B}(\text{OH})_4^-$  on the corrosion resistance of seawater electrocatalysis. The performance of completely unprotected bare Ni-Fe foam rapidly decays in alkaline simulated seawater (black line). The performance decay rate of  $\text{CeO}_2$  coated NiFe foam ( $\text{CeO}_2/\text{NiFe}$ ) electrode in alkaline simulated seawater significantly decreases (blue line), indicating that  $\text{CeO}_2$  has a resistance to chloride ions (Fig. S22b). When the addition of  $\text{BO}_2^-$  to the electrolyte (red line),  $\text{BO}_2^-$  mainly converted to  $\text{B}(\text{OH})_4^-$  in alkaline environments from the Raman result (Fig. S22c). Ni-Fe foam electrode exhibits good corrosion resistance, and surprisingly, the catalytic performance of the electrode had also been slightly improved for enhanced water oxidation. When adding metaborate ions during stability testing, we can observe that the current density rapidly increased for  $\text{CeO}_2/\text{NiFe}$  foam + 1 M KOH + 0.5 M NaCl (green line), indicating that  $\text{BO}_2^-$  can promote the performance of OER. The improvement in OER performance may be attributed to the introduction of  $\text{BO}_2^-$ , which enhances the disturbance of local  $\text{OH}^-$  concentration and facilitates lower  $R_{ct}$  (Fig. S22d) [46]. The above comparison experiment results show that both  $\text{CeO}_2$  and  $\text{BO}_2^-$  have made important contributions to the corrosion resistance and electrocatalytic performance of electrodes. Therefore, it provides a feasible approach for making simple improvements to the current catalytic electrode as an anti-corrosion electrode.

### 3.5. Stability and application

Industrial electrodes often require working at a current density of hundreds of  $\text{mA cm}^{-2}$  for hundreds of hours, which poses a great challenge to the low current density and short-term catalysts currently studied in the laboratory [47]. Hence, we conducted a series of stability tests on this prepared Ni-Fe-Ce-B electrode under various harsh

environments. Fig. S23 illustrates the remarkable stability of the assembled electrolyzer during water electrolysis as the current density increased from 20 to 200 mA cm<sup>-2</sup> in 1 M KOH. As shown in Fig. S24, after 200-h operation at  $\sim 100$  mA cm<sup>-2</sup> under 1.640 V, it can still maintain stable with only slight loss of current density. Moreover, it shows almost no significant decrease in current density after operating for 100 h of  $\sim 200$  mA cm<sup>-2</sup> at 1.740 V. At an industrial current density of  $\sim 500$  mA cm<sup>-2</sup> at 1.816 V, the prepared electrodes can operate stably and maintain about  $\sim 95$  % performance (Fig. 5a), indicating that the prepared electrode material meets the needs of industrial production. From the SEM images of the electrode pairs after the stability test of 100 h of seawater splitting (Fig. S25), the morphology of the electrode surfaces after HER and OER has been partially damaged, which may be caused by the impact of bubbles, water flow, current shock and so on. The density difference before and after stability testing is very small, indicating that its structure has excellent stability (Fig. S26). Moreover, at the same current density, the performance of this electrode in 1 M KOH + natural seawater (from East China Sea) is slightly reduced (Fig. 5b). This is because with the continuous electrolysis, precipitates (Mg(OH)<sub>2</sub> or Ca(OH)<sub>2</sub>) may form on the electrode surface, which may cover active site and reduce the activity of the electrode. Even at higher Cl<sup>-</sup> concentrations under  $\sim 200$  mA cm<sup>-2</sup> (1.760 V), these electrodes can

still maintain a catalytic ability of  $\sim 87.5$  % after 120 h (Fig. 5c). In addition, as the concentration of KOH decreases, the corrosion resistance of the electrode weakens (Fig. S27). This also indicates that the concentration of chloride ions is highly correlated with their corrosiveness. To sum up, evolutionary oxide-anion dual-layer protection mechanism based on Ce-B-containing electrode towards highly corrosive seawater splitting can be summarized as follows. The reactivity of Ce leads to a protective CeO<sub>2</sub> layer, creating an effective barrier against chloride ion corrosion. On the other hand, B on the catalyst surface is dissolved during seawater electrolysis, generating B(OH)<sub>4</sub><sup>-</sup> negative charge layer that repel chloride ions. Consequently, the combined effect of these conditions enhances lifetime catalytic performance of the electrode towards highly corrosive seawater splitting.

Generally, the electrode area for alkaline water electrolysis towards industrial application is usually much larger than that for the laboratory study [48]. However, the preparation methods currently reported in the literatures, such as hydrothermal and calcination methods, are frequently constrained by equipment space limitations. Notably, electrodeless plating offers a viable solution for easily preparing large-area electrode plates as required (Fig. 5d; and Fig. S28). We cut an electrode piece into a 14 cm diameter circular shape, and then assembled a diaphragm free rudimentary alkaline simulated seawater electrolysis

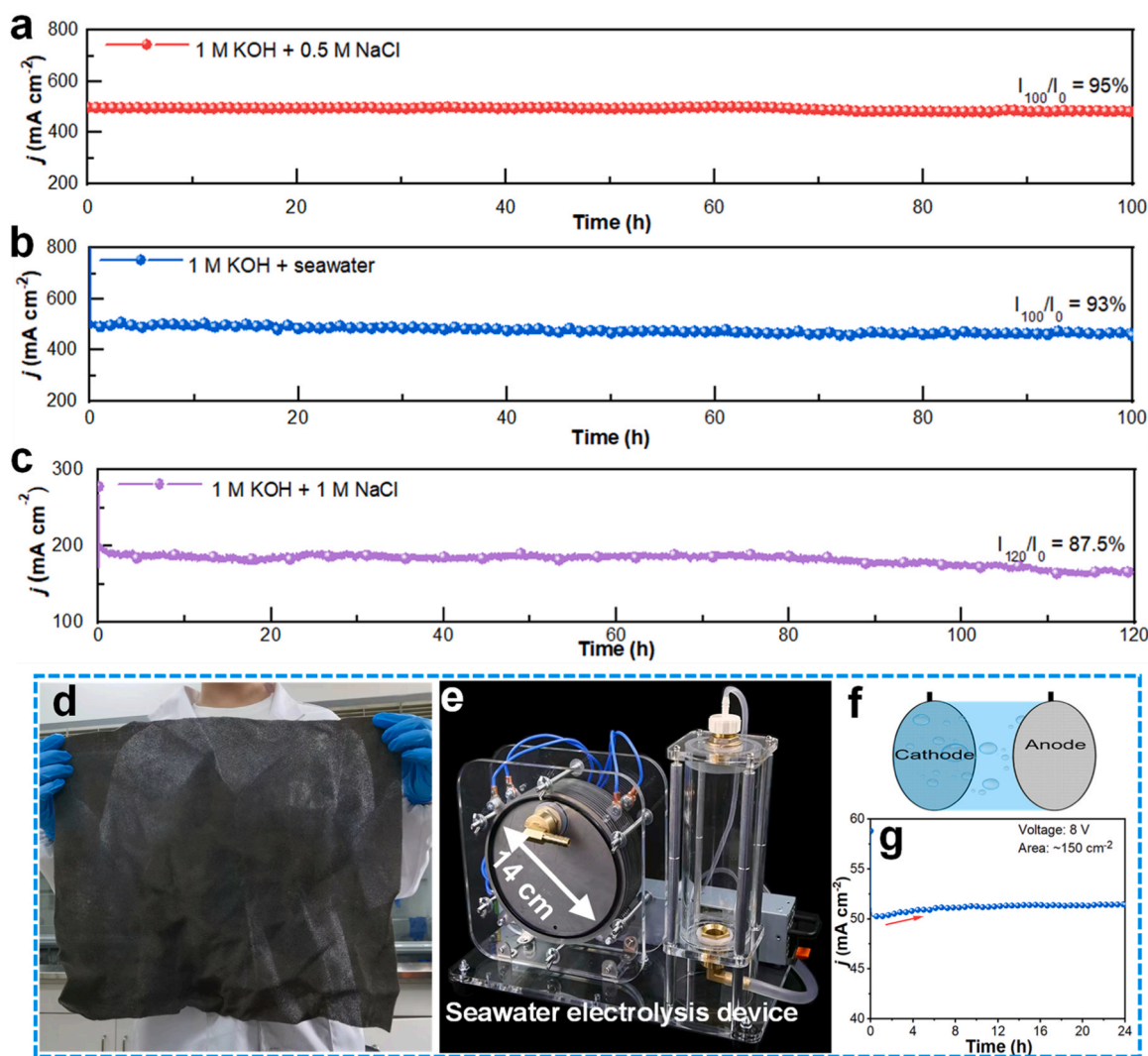


**Fig. 5.** Stability and application. Durability tests of Ni-Fe-Ce-B/MS || Ni-Fe-Ce-B/MS for overall water splitting under 500 mA cm<sup>-2</sup> at 1.816 V in 1 M KOH + 0.5 M NaCl (a), 500 mA cm<sup>-2</sup> at 1.817 V in 1 M KOH + 0.5 M NaCl (b), and 200 mA cm<sup>-2</sup> at 1.740 V in 1 M KOH + 1 M NaCl (c). Optical photos of large area Ni-Fe-Ce-B/MS electrode (d) and self-made seawater electrolysis device (e). (f) Schematic diagram of seawater electrolysis using large-sized electrodes without a diaphragm; (g) 24-h stability of self-made seawater electrolysis at 8 V.

device (Fig. 5e) to measure its stability under a constant voltage of 8 V (Fig. 5f, g). It was observed that after operating for a certain period, the current density increased. This phenomenon is attributed to the reconstruction of the electrode interface, involving changes in electrode surface composition and aggregation of anions at the electrolyte-electrode interface. Furthermore, it is an interesting idea to directly modify this device into a hydrogen-oxygen-welding equipment (Fig. S29).

#### 4. Conclusion

In conclusion, we have innovatively conceived an in-situ dual-layer strategy, incorporating oxide ( $\text{CeO}_2$ ) and anion ( $\text{B}(\text{OH})_4^-$ ), stemming from a Ni-Fe-Ce-B electrode. This novel development is specifically engineered with the primary intent of tackling corrosion caused by chloride ions. During the OER process, Ni, Fe, Ce, and B elements undergo different evolutions in the anode region. The Ni and Fe elements transform into  $\text{NiFeOOH}$ , which predominantly provides the catalytic activity. The Ce element in the catalyst is preferentially oxidized to form a protective  $\text{CeO}_2$  layer outside the electrode, while B dissolves and aggregates as  $\text{B}(\text{OH})_4^-$  anions buffer layer in the electrode-electrolyte interface. The spontaneous in-situ dual-layer system endows the electrode with strong resistance to chloride ions in seawater. Therefore, a low-cost and facile boride electrode achieved notable performance, producing a current density of  $0.5 \text{ A cm}^{-2}$  while maintaining a remarkable durability up to 100 h in 1 M KOH + natural seawater. Intriguingly, the development of Ce-B-containing electrode with dual resistance properties represents a promising avenue for the design and optimization of electrodes that can effectively withstand the harsh environment of seawater electrocatalysis.

#### CRediT authorship contribution statement

**Huixiang Liu:** Experimental measurements, Investigation, Formal analysis, Writing original draft. **Xian Zhou:** Formal analysis, Data curation. **Chuming Ye:** Formal analysis, Data curation. **Mingxin Ye:** Project administration, Conceptualization, Funding acquisition. **Jianfeng Shen:** Project administration, Supervision, Funding acquisition.

#### Declaration of Competing Interest

The authors declare that they have no known competing financial interests or personal relationships that could have appeared to influence the work reported in this paper.

#### Data Availability

Data will be made available on request.

#### Acknowledgements

This work was financially supported by National Natural Science Foundation of China (51972064 and 52222315).

#### Appendix A. Supporting information

Supplementary data associated with this article can be found in the online version at [doi:10.1016/j.apcatb.2023.123560](https://doi.org/10.1016/j.apcatb.2023.123560).

#### References

- [1] L. Wan, Z. Xu, Q. Xu, M. Pang, D. Lin, J. Liu, B. Wang, Key components and design strategy of the membrane electrode assembly for alkaline water electrolysis, *Energy Environ. Sci.* 16 (2023) 1384–1430, <https://doi.org/10.1039/D3EE00142C>.
- [2] H. Xie, Z. Zhao, T. Liu, Y. Wu, C. Lan, W. Jiang, L. Zhu, Y. Wang, D. Yang, Z. Shao, A membrane-based seawater electrolyser for hydrogen generation, *Nature* 612 (2022) 673–678, <https://doi.org/10.1038/s41586-022-05379-5>.
- [3] J.N. Hausmann, R. Schlögl, P.W. Menezes, M. Driess, Is direct seawater splitting economically meaningful? *Energy Environ. Sci.* 14 (2021) 3679–3685, <https://doi.org/10.1039/D0EE03659E>.
- [4] S. Dresch, F. Dionigi, M. Klingenhof, P. Strasser, Direct electrolytic splitting of seawater: opportunities and challenges, *ACS Energy Lett.* 4 (2019) 933–942, <https://doi.org/10.1021/acseenergylett.9b00220>.
- [5] F. Dionigi, T. Reier, Z. Pawolek, M. Glichi, P. Strasser, Design criteria, operating conditions, and nickel-iron hydroxide catalyst materials for selective seawater electrolysis, *ChemSusChem* 9 (2016) 962–972, <https://doi.org/10.1002/cssc.201501581>.
- [6] Y. Kuang, M.J. Kenney, Y. Meng, W.H. Hung, Y. Liu, J.E. Huang, R. Prasanna, P. Li, Y. Li, L. Wang, M.C. Lin, M.D. McGehee, X. Sun, H. Dai, Solar-driven, highly sustained splitting of seawater into hydrogen and oxygen fuels, *Proc. Natl. Acad. Sci. U. S. A.* 116 (2019) 6624–6629, <https://doi.org/10.1073/pnas.1900556116>.
- [7] Z.Y. Yu, Y. Duan, X.Y. Feng, X. Yu, M.R. Gao, S.H. Yu, Clean and affordable hydrogen fuel from alkaline water splitting: past, recent progress, and future prospects, *Adv. Mater.* 33 (2021), 2007100, <https://doi.org/10.1002/adma.202007100>.
- [8] B. Zhang, S. Liu, S. Zhang, Y. Cao, H. Wang, C. Han, J. Sun, High corrosion resistance of NiFe-layered double hydroxide catalyst for stable seawater electrolysis promoted by phosphate intercalation, *Small* 18 (2022), 2203852, <https://doi.org/10.1002/sml.202203852>.
- [9] T. Ma, W. Xu, B. Li, X. Chen, J. Zhao, S. Wan, K. Jiang, S. Zhang, Z. Wang, Z. Tian, Z. Lu, L. Chen, The critical role of additive sulfate for stable alkaline seawater oxidation on nickel-based electrodes, *Angew. Chem. Int. Ed. Engl.* 60 (2021) 22740–22744, <https://doi.org/10.1002/anie.202110355>.
- [10] H.J. Song, H. Yoon, B. Ju, D.-Y. Lee, D.-W. Kim, Electrocatalytic selective oxygen evolution of carbon-coated  $\text{Na}_2\text{Co}_{1-x}\text{Fe}_x\text{P}_2\text{O}_7$  nanoparticles for alkaline seawater electrolysis, *ACS Catal.* 10 (2019) 702–709, <https://doi.org/10.1021/acscatal.9b04231>.
- [11] L. Yu, Q. Zhu, S. Song, B. McElhenny, D. Wang, C. Wu, Z. Qin, J. Bao, Y. Yu, S. Chen, Z. Ren, Non-noble metal-nitride based electrocatalysts for high-performance alkaline seawater electrolysis, *Nat. Commun.* 10 (2019), 5106, <https://doi.org/10.1038/s41467-019-13092-7>.
- [12] W. Xu, T. Ma, H. Chen, D. Pan, Z. Wang, S. Zhang, P. Zhang, S. Bao, Q. Yang, L. Zhou, Z. Tian, S. Dai, Z. Lu, Scalable fabrication of  $\text{Cu}_2\text{S}@ \text{NiS} @ \text{Ni} / \text{NiMo}$  hybrid cathode for high-performance seawater electrolysis, *Adv. Funct. Mater.* (2023), 2302263, <https://doi.org/10.1002/adfm.202302263>.
- [13] Y. Song, M. Sun, S. Zhang, X. Zhang, P. Yi, J. Liu, B. Huang, M. Huang, L. Zhang, Alleviating the work function of vein-like  $\text{Co}_3\text{P}$  by Cr doping for enhanced seawater electrolysis, *Adv. Funct. Mater.* (2023), 2214081, <https://doi.org/10.1002/adfm.202214081>.
- [14] W. Wan, Y. Zhao, S. Wei, C.A. Triana, J. Li, A. Arcifa, C.S. Allen, R. Cao, G. R. Patzke, Mechanistic insight into the active centers of single/dual-atom Ni/Fe-based oxygen electrocatalysts, *Nat. Commun.* 12 (2021), 5589, <https://doi.org/10.1038/s41467-021-25811-0>.
- [15] Z. Yu, Y. Li, V. Martin-Diaconescu, L. Simonelli, J. Ruiz Esquivias, I. Amorim, A. Araujo, L. Meng, J.L. Faria, L. Liu, Highly efficient and stable saline water electrolysis enabled by self-supported nickel-iron phosphosulfide nanotubes with heterointerfaces and under-coordinated metal active sites, *Adv. Funct. Mater.* 32 (2022), 2206138, <https://doi.org/10.1002/adfm.202206138>.
- [16] E. Enkhtuvshin, S. Yeo, H. Choi, K.M. Kim, B.S. An, S. Biswas, Y. Lee, A.K. Nayak, J. U. Jang, K.H. Na, W.Y. Choi, G. Ali, K.H. Chae, M. Akbar, K.Y. Chung, K. Yoo, Y. C. Chung, T.H. Shin, H. Kim, C.Y. Chung, H. Han, Surface reconstruction of Ni-Fe layered double hydroxide inducing chloride ion blocking materials for outstanding overall seawater splitting, *Adv. Funct. Mater.* (2023), 2214069, <https://doi.org/10.1002/adfm.202214069>.
- [17] X. Luo, P. Ji, P. Wang, X. Tan, L. Chen, S. Mu, Spherical  $\text{Ni}_3\text{S}_2/\text{Fe-NiP}_x$  magic cube with ultrahigh water/seawater oxidation efficiency, *Adv. Sci.* 9 (2022), 2104846, <https://doi.org/10.1002/advs.202104846>.
- [18] Q. Yu, X. Liu, G. Liu, X. Wang, Z. Li, B. Li, Z. Wu, L. Wang, Constructing three-phase heterojunction with 1D/3D hierarchical structure as efficient trifunctional electrocatalyst in alkaline seawater, *Adv. Funct. Mater.* 32 (2022), 2205767, <https://doi.org/10.1002/adfm.202205767>.
- [19] J. Liu, S. Duan, H. Shi, T. Wang, X. Yang, Y. Huang, G. Wu, Q. Li, Rationally designing efficient electrocatalysts for direct seawater splitting: challenges, achievements, and promises, *Angew. Chem. Int. Ed. Engl.* 61 (2022) 202210753, <https://doi.org/10.1002/anie.202210753>.
- [20] H. Liu, X. Li, L. Chen, X. Zhu, P. Dong, M.O.L. Chee, M. Ye, Y. Guo, J. Shen, Monolithic Ni-Mo-B bifunctional electrode for large current water splitting, *Adv. Funct. Mater.* 32 (2021), 2107308, <https://doi.org/10.1002/adfm.202107308>.
- [21] K. Aggoun, L. Chaal, J. Creus, R. Sabot, B. Saidani, M. Jeannin, Marine corrosion resistance of  $\text{CeO}_2/\text{Mg}(\text{OH})_2$  mixed coating on a low alloyed steel, *Surf. Coat. Tech.* 372 (2019) 410–421, <https://doi.org/10.1016/j.surfcoat.2019.05.053>.
- [22] W. Tong, M. Forster, F. Dionigi, S. Dresch, R. Sadeghi Erami, P. Strasser, A.J. Cowan, P. Farràs, Electrolysis of low-grade and saline surface water, *Nat. Energy* 5 (2020) 367–377, <https://doi.org/10.1038/s41560-020-0550-8>.
- [23] L. Yu, L. Wu, B. McElhenny, S. Song, D. Luo, F. Zhang, Y. Yu, S. Chen, Z. Ren, Ultrafast room-temperature synthesis of porous S-doped Ni/Fe (oxy)hydroxide electrodes for oxygen evolution catalysis in seawater splitting, *Energy Environ. Sci.* 13 (2020) 3439–3446, <https://doi.org/10.1039/d0ee00921k>.
- [24] J.T. Ren, L. Chen, W.W. Tian, X.L. Song, Q.H. Kong, H.Y. Wang, Z.Y. Yuan, Rational synthesis of core-shell-structured nickel sulfide-based nanostructures for efficient seawater electrolysis, *Small* (2023), 2300194, <https://doi.org/10.1002/sml.202300194>.



- [25] S. Wang, P. Yang, X. Sun, H. Xing, J. Hu, P. Chen, Z. Cui, W. Zhu, Z. Ma, Synthesis of 3D heterostructure Co-doped Fe<sub>2</sub>P electrocatalyst for overall seawater electrolysis, *Appl. Catal. B Environ.* 297 (2021), 120386, <https://doi.org/10.1016/j.apcatb.2021.120386>.
- [26] B. Wang, M. Lu, D. Chen, Q. Zhang, W. Wang, Y. Kang, Z. Fang, G. Pang, S. Feng, Ni<sub>4</sub>Fe<sub>2</sub>N@C microsheet arrays on Ni foam as an efficient and durable electrocatalyst for electrolytic splitting of alkaline seawater, *J. Mater. Chem. A* 9 (2021) 13562–13569, <https://doi.org/10.1039/D1TA01292D>.
- [27] C. Wang, M. Zhu, Z. Cao, P. Zhu, Y. Cao, X. Xu, C. Xu, Z. Yin, Heterogeneous bimetallic sulfides based seawater electrolysis towards stable industrial-level large current density, *Appl. Catal. B Environ.* 291 (2021), 120071, <https://doi.org/10.1016/j.apcatb.2021.120071>.
- [28] Q. Ma, H. Jin, F. Xia, H. Xu, J. Zhu, R. Qin, H. Bai, B. Shuai, W. Huang, D. Chen, Z. Li, J. Wu, J. Yu, S. Mu, Ultralow Ru-assisted and vanadium-doped flower-like CoP/Ni<sub>2</sub>P heterostructure for efficient water splitting in alkali and seawater, *J. Mater. Chem. A* 9 (2021) 26852–26860, <https://doi.org/10.1039/d1ta08699e>.
- [29] Y. Li, X. Wu, J. Wang, H. Wei, S. Zhang, S. Zhu, Z. Li, S. Wu, H. Jiang, Y. Liang, Sandwich structured Ni<sub>3</sub>S<sub>2</sub>-MoS<sub>2</sub>-Ni<sub>3</sub>S<sub>2</sub>@Ni foam electrode as a stable bifunctional electrocatalyst for highly sustained overall seawater splitting, *Electrochim. Acta* 390 (2021), 138833, <https://doi.org/10.1016/j.electacta.2021.138833>.
- [30] H. Zhang, S. Geng, M. Ouyang, H. Yadegari, F. Xie, D.J. Riley, A self-reconstructed bifunctional electrocatalyst of pseudo-amorphous nickel carbide @ iron oxide network for seawater splitting, *Adv. Sci.* (2022), 2200146, <https://doi.org/10.1002/advs.202200146>.
- [31] H. Ren, X. Sun, C. Du, J. Zhao, D. Liu, W. Fang, S. Kumar, R. Chua, S. Meng, P. Kidkhunthod, L. Song, S. Li, S. Madhavi, Q. Yan, Amorphous Fe-Ni-P-B-O nanocages as efficient electrocatalysts for oxygen evolution reaction, *ACS Nano* 13 (2019) 12969–12979, <https://doi.org/10.1021/acsnano.9b05571>.
- [32] J. Liu, Y. Liu, X. Mu, H. Jang, Z. Lei, S. Jiao, P. Yan, M.G. Kim, R. Cao, Boosting activity and stability of electrodeposited amorphous Ce-doped NiFe-based catalyst for electrochemical water oxidation, *Adv. Funct. Mater.* 32 (2022), 2204086, <https://doi.org/10.1002/adfm.202204086>.
- [33] L. Li, X. Cao, J. Huo, J. Qu, W. Chen, C. Liu, Y. Zhao, H. Liu, G. Wang, High valence metals engineering strategies of Fe/Co/Ni-based catalysts for boosted OER electrocatalysis, *J. Energy Chem.* 76 (2023) 195–213, <https://doi.org/10.1016/j.jechem.2022.09.022>.
- [34] P.W. Menezes, A. Indra, C. Das, C. Walter, C. Göbel, V. Gutkin, D. Schmeißer, M. Driess, Uncovering the nature of active species of nickel phosphide catalysts in high-performance electrochemical overall water splitting, *ACS Catal.* 7 (2016) 103–109, <https://doi.org/10.1021/acscatal.6b02666>.
- [35] H. Xu, C. Shan, X. Wu, M. Sun, B. Huang, Y. Tang, C.-H. Yan, Fabrication of layered double hydroxide microcapsules mediated by cerium doping in metal-organic frameworks for boosting water splitting, *Energy Environ. Sci.* 13 (2020) 2949–2956, <https://doi.org/10.1039/D0EE02113J>.
- [36] B. Wu, S. Gong, Y. Lin, T. Li, A. Chen, M. Zhao, Q. Zhang, L. Chen, A unique NiOOH@FeOOH heteroarchitecture for enhanced oxygen evolution in saline water, *Adv. Mater.* 34 (2022), 2108619, <https://doi.org/10.1002/adma.202108619>.
- [37] T. Liu, Y. Chen, Y. Hao, J. Wu, R. Wang, L. Gu, X. Yang, Q. Yang, C. Lian, H. Liu, M. Gong, Hierarchical anions at the electrode-electrolyte interface for synergized neutral water oxidation, *Chem* 8 (2022) 2700–2714, <https://doi.org/10.1016/j.chempr.2022.06.012>.
- [38] C. Jia, C. Zhen, L. Yin, H. Zhu, P. Du, A. Han, G. Liu, H.-M. Cheng, Topologic transition-induced abundant undercoordinated Fe active sites in NiFeOOH for superior oxygen evolution, *Nano Energy* 106 (2023), 108044, <https://doi.org/10.1016/j.nanoen.2022.108044>.
- [39] X. Liu, S. Jing, C. Ban, K. Wang, Y. Feng, C. Wang, J. Ding, B. Zhang, K. Zhou, L. Gan, X. Zhou, Dynamic active sites in NiFe oxyhydroxide upon Au nanoparticles decoration for highly efficient electrochemical water oxidation, *Nano Energy* 98 (2022), 107328, <https://doi.org/10.1016/j.nanoen.2022.107328>.
- [40] H. Sun, X. Xu, Y. Song, W. Zhou, Z. Shao, Designing high-valence metal sites for electrochemical water splitting, *Adv. Funct. Mater.* 31 (2021), 2009779, <https://doi.org/10.1002/adfm.202009779>.
- [41] Z. Huang, X. Liao, W. Zhang, J. Hu, Q. Gao, Ceria-promoted reconstruction of Ni-based electrocatalysts toward efficient oxygen evolution, *ACS Catal.* 12 (2022) 13951–13960, <https://doi.org/10.1021/acscatal.2c03912>.
- [42] Y. Wen, Z. Wei, J. Liu, R. Li, P. Wang, B. Zhou, X. Zhang, J. Li, Z. Li, Synergistic cerium doping and MXene coupling in layered double hydroxides as efficient electrocatalysts for oxygen evolution, *J. Energy Chem.* 52 (2021) 412–420, <https://doi.org/10.1016/j.jechem.2020.04.009>.
- [43] Z. Chen, X. Duan, W. Wei, S. Wang, Z. Zhang, B.-J. Ni, Boride-based electrocatalysts: emerging candidates for water splitting, *Nano Res* 13 (2020) 293–314, <https://doi.org/10.1007/s12274-020-2618-y>.
- [44] N. Wang, A. Xu, P. Ou, S.F. Hung, A. Ozden, Y.R. Lu, J. Abed, Z. Wang, Y. Yan, M. J. Sun, Y. Xia, M. Han, J. Han, K. Yao, F.Y. Wu, P.H. Chen, A. Vomiero, A. Seifitokaldani, X. Sun, D. Sinton, Y. Liu, E.H. Sargent, H. Liang, Boride-derived oxygen-evolution catalysts, *Nat. Commun.* 12 (2021), 6089, <https://doi.org/10.1038/s41467-021-26307-7>.
- [45] R.E. Zeebe, Stable boron isotope fractionation between dissolved B(OH)<sub>3</sub> and B(OH)<sub>4</sub>, *Geochim. Cosmochim. Acta* 69 (2005) 2753–2766, <https://doi.org/10.1016/j.gca.2004.12.011>.
- [46] J. Guo, Y. Zheng, Z. Hu, C. Zheng, J. Mao, K. Du, M. Jaroniec, S.-Z. Qiao, T. Ling, Direct seawater electrolysis by adjusting the local reaction environment of a catalyst, *Nat. Energy* 8 (2023) 264–272, <https://doi.org/10.1038/s41560-023-01195-x>.
- [47] M. Chatenet, B.G. Pollet, D.R. Dekel, F. Dionigi, J. Deseure, P. Millet, R.D. Braatz, M.Z. Bazant, M. Eikerling, I. Staffell, P. Balcombe, Y. Shao-Horn, H. Schafer, Water electrolysis: from textbook knowledge to the latest scientific strategies and industrial developments, *Chem. Soc. Rev.* 51 (2022) 4583–4762, <https://doi.org/10.1039/d0cs01079k>.
- [48] M.F. Lagadee, A. Grimaud, Water electrolyzers with closed and open electrochemical systems, *Nat. Mater.* 19 (2020) 1140–1150, <https://doi.org/10.1038/s41563-020-0788-3>.